Reconstruction of the 3D velocity field of the two-phase bubbly flow around a half moon obstacle Using wire-mesh sensor data

Al Issa[a] S., Beyer[a] M., Prasser[b] H.-M., Frank[c] Th.

[a]Forschungszentrum Dresden-Rossendorf e.V., Institute of Safety Research, P.O. Box 510 119, D-01314 Dresden, Germany
[b]Eidgenössische Technische Hochschule Zürich, ML K 13, Sonneggstrasse 3, CH-8092, Zürich, Switzerland
[c]ANSYS Germany, CFX Development, Staudenfeldweg 12, D-83624 Otterfing, Germany
S.Alissa@fz-rossendorf.de, hprasser@ethz.ch, Thomas.Frank@ansys.com

Keywords: 3D velocity field, two-phase flows, obstacle, CFD

Abstract

The TOPFLOW facility at Forschungszentrum Dresden-Rossendorf (FZD) is used to investigate two-phase upward flows in 50 mm diameter and 200 mm diameter pipes. The facility enables conducting Experiments with air-water and steam-water flows for temperature range of 35-280 °C and pressure range of 1-70 bar. The test pipes are equipped with a wire-mesh sensor, which is a conductivity-based void fraction sensor developed by FZD. It provides void fraction measurements in a matrix of 64×64 points and a measuring frequency of 2.5 kHz. CFD models have to demonstrate their validity in geometries, where phenomena like flow separation, recirculation regions, stagnation points, free jet formation and similar are present. In the experiment described in this paper the flow around an asymmetric, half-moon shaped obstacle put into the large vertical test section of TOPFLOW is studied. In order to obtain information in three dimensions, the obstacle was traversed along the pipe axis. In this way, it was possible to record 2D void fraction distributions at different distances upstream and downstream of the obstacle using a stationary wire-mesh sensor. The fact that the high resolution data supplied by the sensor contains information on all individual bubbles that cross the measuring plane gives the opportunity to extract more detailed information on the flow structure. In particular, from the transit time of bubbles through the sensor plane approximate axial profiles of the liquid velocity were obtained. The lateral movement of the 2D image of bubbles in the measuring plane during their passage was evaluated to reconstruct 2D velocity fields in the environment of the obstacle. In this way, a full three-dimensional vector field of the velocity was provided for code validation. The paper presents the methods of data evaluation, an assessment of the obtained accuracy of the velocity estimation, experimental results and a comparison to the results of CFD calculations.

Introduction

Multidimensional two-phase flows appear in many industrial applications. One of the main and important applications is power plants, either fossil or nuclear. The efficient and safe design of a power plant often requires the knowledge of three-dimensional two-phase flow fields. CFD codes have reached maturity for single phase applications, while the models development and validation for two-phase flows still in advance. Closure laws that describe the interactions between phases, such as momentum and energy transfer; as well as the code in its full complexity need to be validated against experiments.

Prominent examples for three-dimensional flows are found in constrictions, (such as expansions, contractions…etc), flows over obstacles and through valves. The flow structure in these flows is complex and characterised by steep velocity gradients, turbulence, recirculation, detachment and reattachment of the flow, in addition to redistribution of gaseous phase.

The aim of this paper is to provide data for CFD code validation for two-phase cases of strong three-dimensional nature, where the mentioned phenomena occur. This requires experimental techniques and special instrumentation that are able to record a 3D data set. The gas-liquid flow around an asymmetrical, half-moon shaped obstacle equipped into a vertical pipe is chosen. . Special attention is given to the evaluation of the applied wire-mesh sensor void fraction measurements. A novel data evaluation method is introduced that allows extracting approximate three-dimensional velocity field upstream and downstream of the constriction caused by the obstacle.

Nomenclature

A	Area (m^2)
a	Weighting factor
b	Bubble identification number
C	Calibration factor
D	Diameter (m) or (mm)
f	Data acquisition frequency (frame s^{-1})
H	Probability (%/m^{-1})
i,j	Coordinates Indexes in a cross section
J	Superficial velocity
k	Time coordinate
n	Bubble number
t	Time (s)
V	Volume (mm^3)
v,w	Velocity (ms^{-1}) or (mm s^{-1})
x,y,z	Cartesian coordinates (m) or (mm)

Greek letters
ε   Void fraction
Δ   Difference
Subsripts
bub   Bubble
CM   Centre of mass
Equ   Equivalent
G   Gas
i,j   Coordinates Indexes in a cross section
k   Time coordinate
L   Liquid
MB   Marker bubble
max   Maximum
n   Bubble number
x,y   Cartesian coordinates

Literature review

Single and two-phase flows of three-dimensional nature were subject of numerous studies found in literature. Most of them dealt with flows around obstacles or, respectively, through a sudden expansion or constrictions in general. Similar flow fields are found in many engineering applications, like nuclear reactors, chemical reactors and power plants in general. A prominent example is the steam-water flow in safety valves described by Nishimura et al. (2000) and Boccardi et al. (2004). One of the general characteristic of these flows is the formation of vortexes and recirculation zones downstream of the obstacle. The majority of the works aims at the prediction of the flow field and its main features like length, reattachment point, void fraction and velocity field distributions on basis of different modelling approaches. Experiments are carried out in order to validate the proposed models. Concerning the choice of the fluid, single-phase liquid flow experiments are presented by Anagnostopoulos et al. (2004) and Sotiriadis et al. (2005), gas-liquid two-phase studies are found in Rinne et al. (1996), Nishimura et al. (2000), Morel et al. (2004), Boccardi et al. (2004), Kondo et al. (2002, 2004, 2005) and Ahmed et al. (2005), a pure gas wind channel experiment is given in Ota et al. (2001) and particulate liquid-solid flows are subject of Founti et al. (2001). Some papers deal with practical problems, like the determination of the capacity of safety valves (Nishimura et al., 2000 and Boccardi et al., 2004) and wear in particle laden oil flows (Founti et al., 2001). Details of the flow field downstream the geometry change are obtained by LDA (Founti et al., 1998; Sotiriadis et al., 2005) and PIV (Anagnostopoulos et al., 2004) or, alternatively, by hot-film and hot wire anemometers (Founti et al., 2001, Morel et al., 2004 and Ahmed et al., 2005). The gas fraction and the structure of the two-phase flow are measured by local probes (Kondo et al., 2002 and Morel et al., 2004) and high-speed camera observation by Rinne et al. (1996), Kondo et al. (2002) and Ahmed et al. (2005). In all cases, except the wind channel (Ota et al., 2001); the flow domain has a characteristic scale of 25 - 100 mm. There are no experiments published dealing with high resolution measurements of the flow field in gas-liquid two-phase flows at higher pressures and temperatures. It is a unique feature of TOPFLOW to combine a comparatively large scale with the ability to perform experiments with steam-water mixture at up-to 7 MPa.

From the shape of the cross-section change, a stepwise expansion dominates in the literature, because the recirculation areas forming downstream present a challenge to the modelling. In one case, a movable piston was applied to create a periodically changing cross-section obstruction Anagnostopoulos et al. (2004). The idea of the movable obstacle in our tests is different from this methodology, since here the change of the position of the obstacle is used to vary the distance between obstacle and sensor in order to obtain 3D parameter fields, and not the degree of obstruction.

Concerning modelling and simulation, different mathematical approaches were used or the numerical simulation, like own implementations of the SIMPLE algorithm in Agnostopoulos et al. (2004), Eulerian particle tracing (Founti et al., 1998, 2001 and Kondo et al., 2002, 2004, 2005) including collision modelling (Founti et al., 1998), two-fluid models (Morel et al., 2004), Large eddy Simulation, commercial CFD codes like CFX (Prasser et al., 2004c) and NEPTUNE by Morel et al. (2004). 3D modelling of two-phase flows showed the importance of the correct reflection of the forces acting on bubbles according to their diameter. The need to represent measured data in 3D appeared in most cases. Sometimes symmetry properties, like radial symmetry, were used to concentrate on radial profiles. With our own experiments we faced the challenge to create a complex three-dimensional flow field and to characterize it by a 2D measuring sensor, which was indirectly traversed along the flow direction by moving the obstacle.

Particular results concerning the behaviour of the flow field downstream of an expansion are worth mentioning: In a horizontal flow and a liquid-particle flow it was found that a second recirculation may happen far from the sudden expansion (Founti et al., 2001 and Anagnostopoulos et al., 2004), the reattachment point was dependent on particle loading (Founti et al., 1998). A similarity to the influence of the void fraction in our case can be expected. The reattachment distance also was related to the obstacle dimensions (Ota et al., 2001 and Sotiriadis et al., 2005). The movement and behaviour of bubbles incorporated many phenomena. The bubbles were deformed and broken by a strong liquid shear field. Also they were not driven to the wall after the expansion as an expected effect of the shear layer, which is a result of the change of the sign of the lift force coefficient (Kondo et al., 2005). Bubble entrainment into recirculation zones was dependent on the Stokes number (Founti et al., 1998), sometimes they were trapped in the recirculation zone (Founti et al.,2001), but they were escaping in case of the occurrence of a large vortex and large fluxes (Kondo et al., 2005). If the flow contains slugs, those are broken up on their way through the expansion. This changes the flow pattern from slug to bubbly flow (Kondo et al., 2005 and Ahmed et al., 2005). This phenomenon becomes dominating at large superficial velocities (Kondo et al., 2002). The effect of the bubble diameters on the interfacial area forces was demonstrated by Morel et al. (2004) and Kondo et al. (2004). The motion of small bubbles at high superficial liquid velocities needs further investigation (Kondo et al., 2005). An increase in the liquid velocity, turbulence and drift velocities were marked in Ahmed et al. (2005), the deformation of the flow is conserved up-to large distances from the cross-section change and was still found even far from the reattachment point (Ota et al., 2001, Kondo et al., 2002 and Ahmed et al.,

2005). This implies that the ordinary flow regime map, which was elaborated to characterise the two-phase flow in a straight channel, may be inapplicable to complex 3D two-phase flow, and some modification should be considered in Kondo et al. (2002). The intensity of reverse and lateral flows was marked in Ota et al. (2001).

Experiments set-up and conditions

The experiments were performed at the vertical test section of TOPFLOW (Two Phase FLOW Test Facility) (Schaffrath et al. 2001) at the Institute of Safety Research of Forschungszentrum Dresden-Rossendorf e.V. The test pipe (figure 1, left), has an inner diameter of 195.3 mm and a total height of 9 m (L/D=45). Water is supplied from the bottom with a maximum flow rate of 50 kg/s. The two-phase flow is generated by feeding gas through an injector consisting of 16 radial tubes with a total number of 152 orifices of 0.8 mm

diameter, connected to a conical head placed in the centre of the pipe (figure 1, middle).

Because it is not possible to design a movable wire-mesh sensor, the other way around was applied: the sensor remains stationary and the obstacle - a half-moon obstacle – is moved up and down in the vertical test section (figure 1, right). This setup will allow the measurement of the three-dimensional gas fraction field around the obstacle for air-water and steam-water experiments up to the maximum pressure of TOPFLOW. The field can be measured both upstream and downstream of the obstacle, since the installation shown in figure 1 can either be flanged from below or from above after inverting it. The obstacle has is a half-moon shaped plate, the straight edge of it is arranged along the diameter of the pipe, while the circular edge is in a distance of 10 mm from the inner wall of the pipe. The obstacle is mounted on top of a toothed rod connected to a translation mechanism to change the axial position of the obstacle.
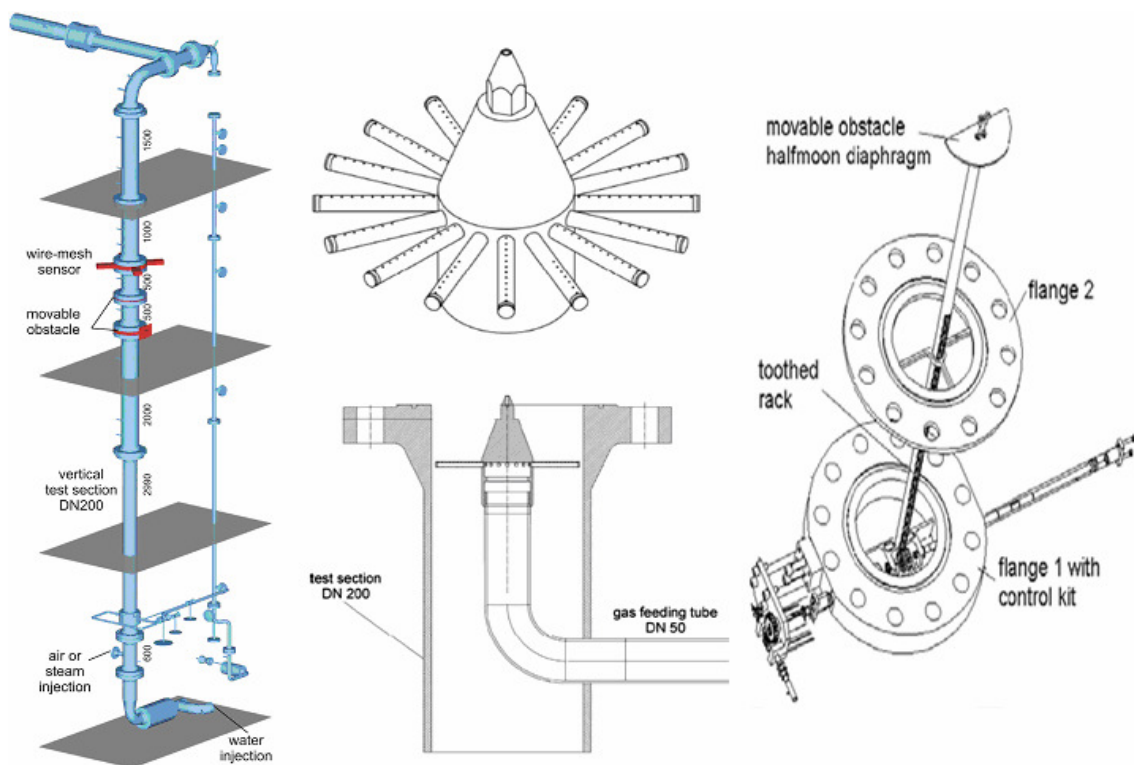

Figure 1: Left: Test section with obstacle and wire-mesh sensor. Middle: injection device –top- and mixing device –bottom- Right: the half moon obstacle with driving mechanism.

The sensor was located 6.17 m downstream of the gas injection, when the asymmetric obstacle was put upstream of the sensor. When the obstacle was put downstream of the sensor, the distance was 5.11 m. The described arrangement allows acquiring local instantaneous void fractions from the full cross-section of the pipe with a spatial resolution of 3 mm and a rate of 2.5 kHz within the three-dimensional flow field around the obstacle. The distance between sensor and obstacle can be varied from 10 mm to a maximum distance of 520 mm without moving the sensor position, which is essential to perform high-pressure experiments in an efficient way, i.e. without dismantling and rearranging the test facility each time the measuring position has to be changed.

Measurements were carried out in an air-water flow at ambient pressure and a temperature about 30 °C as well as in a steam-water mixture under saturation conditions at 6.5 MPa

and 281 °C. A test matrix corresponding to different liquid and gas superficial velocities was executed. However this paper concentrates on point 074 (J_L=1.017 m/s J_G=0.0368 m/s) which lies in a bubbly flow regime. In order to study the two-phase flow around the obstacle the distance between obstacle and wire-mesh sensor was varied as follows: ± 520 mm, ± 250 mm, ± 160 mm, ± 80 mm, ± 40 mm, ± 20 mm, ± 15 mm, ± 10 mm.

Measurements were obtained by the wire-mesh sensor which is a conductivity-based void-fraction sensor. It consists of two planes of 64 x 64 orthogonal wires corresponding to 3260 measuring points over the cross-section. The diameter of the wires: 250 μm, distance between the wires: 3 mm as well as between the two wire-planes. Every wire is electrically insulated against the remaining wires and against the body of the sensor. At each measuring point, the electrical

conductivity between the transmitter and the receiver wires of the circumfluent medium is determined. These analogue values are sampled and converted by a special electronic device connected to the sensor. After the measurement, the digital data is saved on a PC where it is stored for further processing. In order to get sufficient information for the assessment of the flow structure; the measurements are carried out for 10 seconds under steady state conditions with the maximum frequency of 2500 frames per second.

CFX Pre-Test calculation

Before the experiments were performed a pre-test calculation was done for the boundary conditions of the air-water test point 074. Flow conditions correspond to the bubbly flow regime. CFD simulation was done using ANSYS CFX 10.0. The Eulerian two-phase flow model was used, assuming that the gaseous phase consists of monodisperse bubbles with a pipe elevation dependent equivalent diameter of 4.8-5.2 mm in order to account for the hydrostatic bubble expansion. Both phases were treated as non-compressible. Bubble drag in accordance to Grace Drag law, Tomiyama lift force, Frank's generalised wall lubrication force (Frank 2005) and the FAD turbulent dispersion force have been taken into account. Bubble coalescence and fragmentation were neglected for this first pre-test simulation, also it can be assumed that bubble fragmentation will take place at the edges of the obstacle and coalescence might become of importance in regions of bubble accumulation i.e. in the wake behind the obstacle. Steady state simulations with ANSYS CFX 10.0 were performed on two numerical meshes created with ICEM CFD Hexa and consisting of about 119.000 and 473.000 hexahedral mesh elements. Meshes were generated for half of the TOPFLOW geometry assuming axial symmetry. The flow domain for the CFD simulation consists of two 1.5 m long pipe sections upstream and downstream the obstacle. Inlet boundary conditions were set to fully-developed two-phase pipe flow profiles for air and water velocities, radial gas volume fraction distribution, turbulent kinetic energy and turbulent eddy frequency. At the outlet cross section of the 3.0 m long pipe section an averaged static pressure outlet boundary condition was used

Evaluation of wire-mesh sensor data

Time averaged void fraction distributions

The wire-mesh sensor supplies a time sequence of instantaneous local gas fraction distributions within the measuring plane. At each crossing point of wires belonging to different electrode planes of the sensor a control volume with the indexes i, j is formed, from which a gas fraction value $\varepsilon_{i,j,k}$ is delivered for each time sample k. The relation between the indexes i, j, k and the coordinates as well as the time are:

$$x = i \cdot \Delta x; \ y = j \cdot \Delta y; \ t = k \cdot \Delta t \ = k/f_{sample} \ (1)$$

When the local values are averaged over the total measuring time (in this case 10 s, or, respectively, from k = 1 to k = k_{max}), a two-dimensional void fraction distribution is obtained:

$$\bar{\varepsilon}_{i,j} = \frac{1}{k_{max}} \sum_{k=1}^{k_{max}} \varepsilon_{i,j,k} \ (2)$$

If it is assumed that the translation of the obstacle with respect to the sensor position can be approximately envisaged as a scan of the 3D void distribution around the obstacle, then the distributions measured for each of the distances can be combined to result in a full 3D void fraction field around the obstacle.

Bubble size distribution

Due to the fine spatial resolution it is possible to identify individual bubbles in the sensor signal. A bubble is a region of interconnected gas containing elements of the data array $\varepsilon_{i,j,k}$ that is surrounded by elements filled with the liquid phase. The operation of the bubble identification described in Prasser et al. (2001) results in a second three-dimensional array $b_{i,j,k}$, which assigns unique identification numbers specific for each bubble to each element of the distribution $\varepsilon_{i,j,k}$.

Both arrays $\varepsilon_{i,j,k}$ and $b_{i,j,k}$ are used to calculate equivalent diameters of the bubbles. The volume of a bubble with the identification number n is calculated as follows:

$$V_{bub,n} = \Delta x \Delta y \Delta t \cdot w_{bub} \sum_{i,j,k} \varepsilon_{i,j,k} \quad \forall [i,j,k]: b_{i,j,k} = n \quad (3)$$

This volume can be transformed into an equivalent diameter of the bubble:

$$D_{equ,n} = \sqrt[3]{\frac{6V_{bub,n}}{\pi}} \quad (4)$$

As it can be seen from equation (3), the extraction of a volume-equivalent diameter D_{equ} requires information about the bubble velocity. This is necessary to specify the extension of the control volume formed by a crossing point of electrode wires of the sensor, which is equal to the area $\Delta x \cdot \Delta y$ within the measuring plane, multiplied by the distance the bubble travels during the sampling period Δt, which is equal to $\Delta t \cdot w_{bub}$. If the bubble velocity is not available, the size of the bubbles can be characterized by the diameter of a circle D_{xy} equivalent to the maximum area occupied by the bubble in the measuring plane during its passage through the sensor. The equivalent bubble diameter D_{xy} characterizes the lateral extension of a bubble (Prasser et al., (2005a) and Pietruske et al., (2005)). The area occupied by a bubble at an instant given by the index k is

$$A_{xy,n,k} = \Delta x \Delta y \sum_{i,j} \varepsilon_{i,j,k} \quad \forall [i,j,k]: b_{i,j,k} = n \quad (5)$$

The equivalent diameter in the x,y-plane is calculated from the maximum area:

$$D_{xy,n} = \sqrt{\frac{4A_{xy,n,max}}{\pi}} \quad where \quad A_{xy,n,max} = max(A_{xy,n,k}) \quad (6)$$

The equivalent diameter D_{xy} is an alternative to the diameter of the equivalent sphere for characterizing the structure of the two-phase flow, when the bubbles velocity is not available. Bubble size distributions are constructed by integrating the gas fraction carried by each individual bubble over classes of bubble diameters. These histograms represent distributions of the partial void fraction over the bubble diameter. Their unit is 1/mm or %/mm:

$$H_{bub} = \frac{d\varepsilon}{dD_{xy}} = f(D_{xy}), \quad [\% / mm] \quad (7)$$

Liquid velocity profile

There is a way to assess time-averaged liquid velocity distributions by evaluating the transit time of bubbles through the measuring plane of the sensor. For a hypothetical spherical bubble shape, the diameter in all three co-ordinate directions would be identical. The deviation from the spherical shape can be taken into account by a calibration factor C. On basis of the bubble identification algorithm and the bubble diameter measurement described in the previous section, the bubble velocity can be expressed as follows:

$$w_{bub,n} = C \cdot \left(\frac{D_{xy,n}}{\tilde{D}_{equ,n}} \right)^3 = C \cdot \tilde{w}_{bub,n} \qquad (8)$$

Where $\tilde{D}_{equ,n} = \sqrt[3]{\dfrac{6\tilde{V}_{bub,n}}{\pi}}$ is an auxiliary equivalent diameter,

calculated without involving the bubble velocity, i.e. $\tilde{V}_{bub,n} = \Delta x \Delta y \Delta t \sum_{i,j,k} \varepsilon_{i,j,k} \quad \forall [i,j,k] : b_{i,j,k} = n$. The dimension of $\tilde{D}_{equ,n}$ is $(mm^2 \cdot s)^{1/3}$. In equation (8) $\tilde{w}_{bub,n}$ is the bubble velocity without the correction accounting for the deviation from the spherical shape.

The degree of deformation of a bubble depends on the bubble size, when the physical properties of the fluids are constant. For bubbles from a narrow region of equivalent diameters of $D_{MB,1} \le D_{xy} \le D_{MB,2}$, which we call "marker bubbles", it can be assumed that the calibration factor C is nearly constant and independent of the location within the measuring plane. The same holds for the rise velocity of the bubbles Δw_{bub} relative to the liquid velocity. A time-averaged two-dimensional velocity distribution of the marker bubbles is found using the local instantaneous gas fraction as a weight function. Those elements that belong to bubbles outside the size interval defined for marker bubbles are ignored:

$$\overline{w}_{MBi,j} = \frac{1}{\overline{\varepsilon}_{i,j} \cdot k_{max}} \sum_{k=1}^{k=k_{max}} \begin{cases} \tilde{w}_{bub,i,j,k} \cdot \varepsilon_{i,j,k} & if \quad D_{MB1} \le D_{xy,i,j,k} \le D_{MB2} \\ 0 & elsewhere \end{cases} \qquad (9)$$

Due to the approximate constancy of the calibration factor and the bubble rise velocity, the local time averaged liquid velocity can be written as follows:

$$\overline{w}_{L,i,j} = C \cdot \overline{w}_{MB,i,j} - \Delta w_{bub} \qquad (10)$$

In equation (10) all deviations of the bubble rise velocity relative to the liquid phase due to local acceleration of the fluid as well as bubble swarm effects are neglected. In a strict sense, equation (10) is valid only for bubbles rising in still liquid at low void fractions. It was decided not to account for these effects and to restrict the evaluation to an approximate assessment of the liquid velocity and the velocity distributions, because the assumption of the constancy of the calibration factor for itself is a quite rough approach leading to large uncertainties. An assessment of uncertainty of the obtained velocity profiles is discussed in a separate section.

The calibration factor can be obtained by reconstructing the interfacial liquid velocity from the two-dimensional profiles of velocity and gas fraction and comparing the result to the known superficial liquid velocity in the test pipe:

$$J_L = \sum_{i,j} a_{i,j} \cdot \overline{w}_{L,i,j} \cdot \left(1 - \overline{\varepsilon}_{i,j} \right) = \left\langle \overline{w}_{L,i,j} \cdot \left(1 - \overline{\varepsilon}_{i,j} \right) \right\rangle \qquad (11)$$

Where $a_{i,j}$ are weight factors defining the share of the total measuring plane which is represented by the local control volume of the sensor with the indexes i,j. The symbol $\left\langle \ \right\rangle$

denominates a spatial averaging over the measuring plane. For an arbitrary quantity x distributed over the measuring cross-section, the averaging is performed as follows:

$$\left\langle x_{i,j} \right\rangle = \sum_{i,j} a_{i,j} \cdot x_{i,j} \qquad (12)$$

The calibration factor can be made explicit by the combining of equations. (10) and (11),

$$C = \frac{J_L + \Delta w_{bub} \left(1 - \left\langle \overline{\varepsilon}_{i,j} \right\rangle \right)}{\left\langle \overline{w}_{MB,i,j} \right\rangle - \left\langle \overline{w}_{MB,i,j} \cdot \overline{\varepsilon}_{i,j} \right\rangle} \qquad (13)$$

After the calibration, a liquid velocity distribution is calculated using equation (10). The calibration factor can only determined in the described way when the two-dimensional measuring plane is free from regions with flow reverse. In case of the experiments with the movable obstacle, this can be guaranteed only when the sensor was located upstream the obstacle. As it will be shown later, the flow downstream of the half-moon shaped plate was affected by a large recirculation area. Since the marker bubble method does not distinguish between upwards and downwards motion of bubbles, in both cases, always a positive velocity is measured. In the re-circulation region, the superficial liquid velocity is therefore overestimated by equation (11) and, consequently, the calibration factor is underestimated. For this reason, the calibration according to equation (13) was performed only for negative distances between sensor and obstacle, namely for Δz= -520, -250, -160, -80, -40, -20, -15, -10 mm. The individual calibration factors were averaged and the average factor was applied also for the positive distances Δz = 10, 15, 20, 40, 80, 160, 250, 520 mm .In order to keep the bubble deformation and the bubble rise velocity in a narrow band, the interval for the diameter of the marker bubbles was set to 4 - 5 mm. This is a compromise between the tendency to make marker bubbles as small as possible to approach the spherical shape as much as possible, and the advantage of bubbles around 6 mm equivalent diameter, for which the rise velocity is nearly bubble-size independent. Another reason is statistical, i.e. the limits have to be defined in a way, that there are still enough bubbles found in the in the selected interval.

Assessment of lateral bubble velocities

The attempt was made to get a rough estimate for the movement of the bubbles within the measuring plane of the sensor. Due to the asymmetric obstruction of the pipe, the flow cannot be considered axially parallel, i.e. significant lateral components for both gas and liquid velocities have to be expected, which are most pronounced in the direct vicinity of the obstacle. In fact, a visualization of time sequences of two-dimensional instantaneous gas fraction distributions captured by the wire-mesh sensors show lateral movements of the bubbles while they cross the measuring plane. Unlike the estimation of the axial velocity which needed the use of the marker-bubble method described above, the estimation of the lateral velocity of a bubble was made by directly tracking the transversal movement of the centre of mass of its two-dimensional image. When a bubble passes the measuring plane, it will be imaged in several slices. Each slice corresponds to a measuring time step k. The points belonging to a specific bubble are identified by the bubble number n, i.e. an element with the indices i,j,k belongs to bubble n if $b_{i,j,k} = n$. The centre of mass of each slice of the

bubble can be found by averaging the x and y coordinates of each element that belongs to the given bubble weighted by the local instantaneous gas fraction $\varepsilon_{i,j,k}$:

$$x_{CM,n}(t) = \frac{\sum\limits_{\forall i,j:b_{i,j,k}=n} \varepsilon_{i,j,k} \cdot i \cdot \Delta x}{\sum\limits_{\forall i,j:b_{i,j,k}=n} \varepsilon_{i,j,k}}$$

(14)

$$y_{CM,n}(t) = \frac{\sum\limits_{\forall i,j:b_{i,j,k}=n} \varepsilon_{i,j,k} \cdot j \cdot \Delta y}{\sum\limits_{\forall i,j:b_{i,j,k}=n} \varepsilon_{i,j,k}}$$

Where $t = k \cdot \Delta t$. The components $v_{x,n}$ and $v_{y,n}$ of the velocity of bubble n are found by a linear regression of the available time sequence of coordinates of the centre of mass during the bubble passage. The result of the linear fit is presented in the form

$$x_{CM,n}(t) = v_{x,n} \cdot t + c_x$$

$$y_{CM,n}(t) = v_{y,n} \cdot t + c_y$$

(15)

where the constants c_x and c_y are meaningless. To obtain an average gas velocity in every point (i,j) of the plane, a void-fraction weighted time-averages of these two quantities were calculated over all bubbles found during the total measuring period ($t_{meas} = 10$ s $= k_{max} \cdot \Delta t$):

$$\overline{v}_x(i,j) = \frac{1}{\sum\limits_{k=1}^{k_{max}} \varepsilon_{i,j,k}} \cdot \sum\limits_{k=1}^{k_{max}} \left\{ \begin{matrix} \varepsilon_{i,j,k} \cdot v_{x,b_{i,j,k}} \; if \; b_{i,j,k} \neq 0 \\ 0 \; if \; b_{i,j,k} = 0 \end{matrix} \right\}$$

(16)

$$\overline{v}_y(i,j) = \frac{1}{\sum\limits_{k=1}^{k_{max}} \varepsilon_{i,j,k}} \cdot \sum\limits_{k=1}^{k_{max}} \left\{ \begin{matrix} \varepsilon_{i,j,k} \cdot v_{y,b_{i,j,k}} \; if \; b_{i,j,k} \neq 0 \\ 0 \; if \; b_{i,j,k} = 0 \end{matrix} \right\}$$

The resulting time-averaged velocities provide an estimation of the lateral velocity field. This calculation was made for all available distances upstream and downstream of the obstacle.

Experimental Results

General observations

The flow field found in the air-water case at test-point 074 is shown in figure 2. The figure presents void fraction and axial velocity distributions at a plane that represents a central cut along the pipe axis, perpendicularly to the linear edge of the half-moon shaped obstacle. Furthermore, a two-dimensional distribution in each of the 16 measuring planes is given.

The undisturbed flow at the conditions of this test is characterized by a wall peak of the void fraction profile, which can be found up to the axial position 160 mm upstream of the obstacle. 80 mm upstream of the obstacle, the

influence of the cross-section obstruction becomes evident. The velocity profile becomes asymmetric with a more and more pronounced maximum on the unobstructed side.

On the front side of the obstacle a stagnation point is clearly visible in the velocity plot. In the same time, this region shows a local minimum of the void fraction. On the curved stream lines upstream of the stagnation point, the fluid experiences a strong acceleration. In the result, the heavier phase, i.e. the water, is accumulated and the gaseous phase is moved out of the stagnation region.

High velocities are found both in the unobstructed part of the pipe cross-section as well as in the 10 mm wide gap between the circular edge of the obstacle and the pipe wall on the other side. The flow separates from the edge of the obstacle and a high velocity jet downstream of the obstacle is formed. On the side of the unobstructed half of the cross-section, the jet ranges beyond the end of the measuring domain, i.e. the equilibrium profile found 520 mm upstream of the obstacle is not re-established to the distance of 520 mm downstream of the obstacle. Fully developed flow profiles require an inlet length of significantly more than L/D = 2.5 to establish. A velocity peak is also found downstream of the 10 mm wide circular gap between obstacle and pipe wall on the side opposite to the main jet, though this maximum vanishes after about L/D = 1. The elliptical region with a local velocity maximum at about L/D = 0.5 straight above the obstacle is a recirculation area. This can be deduced from the superficial liquid velocities calculated using equation (11). When this value is plotted as a function of the axial location, it is found that the reconstructed superficial velocity significantly exceeds the set value of the test (see figure 8).

Note that the calibration coefficient was kept constant and equal to the value obtained as an average for all level upstream of the obstacle (where recirculation regions can be excluded). The maximum is caused by the fact that the marker bubble method is not sensitive to the direction of the bubbles. The bubble velocities estimated by relating the lateral extension of the bubbles to their passage time are always positive. Therefore, in a recirculation area a local maximum is found. If a part of the cross section is affected by downwards flow, the volume flow rate in this region is added to the flow rate in the upwards flow region and the reconstructed superficial velocity is systematically overestimated.

Within the recirculation area, a strong accumulation of the gaseous phase is observed. Close to the obstacle (at z = 20 mm), the gas accumulation covers almost the entire backside of the half-moon shaped plate. More downstream, the bubbles are transported towards the central region of the pipe, where the absolute maximum of the void fraction is found at z = 160 mm.

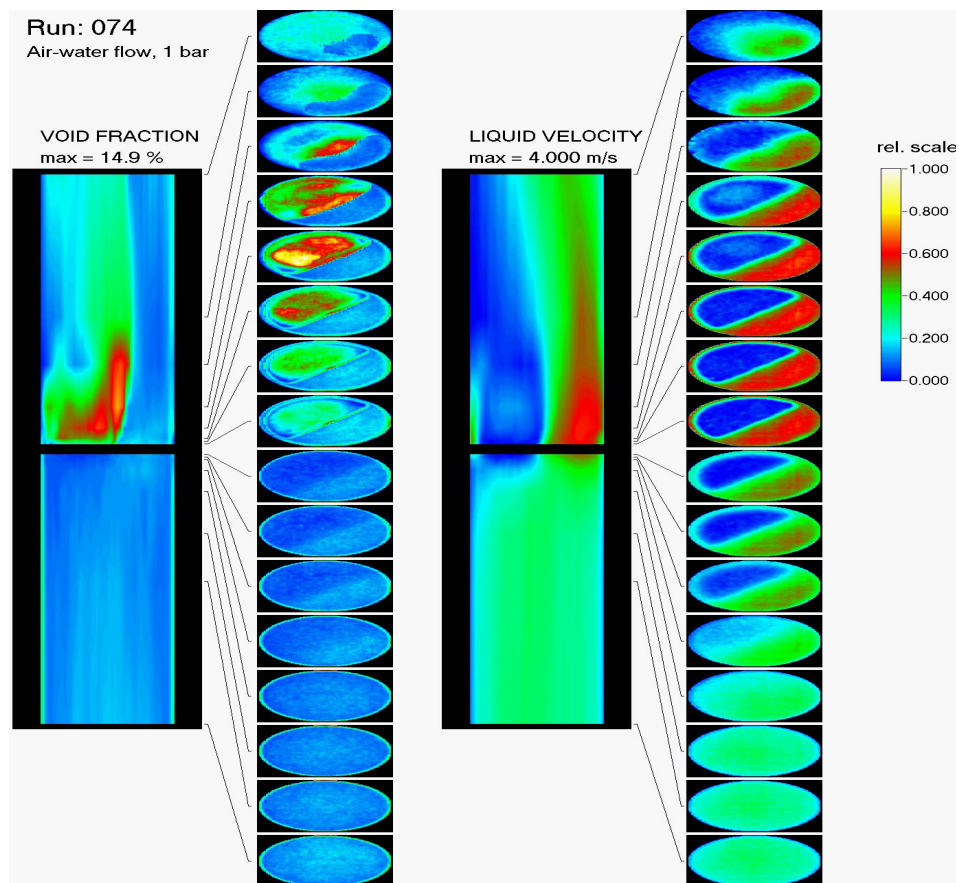**Figure 2:** Void fraction and liquid velocity distributions in the air-water test
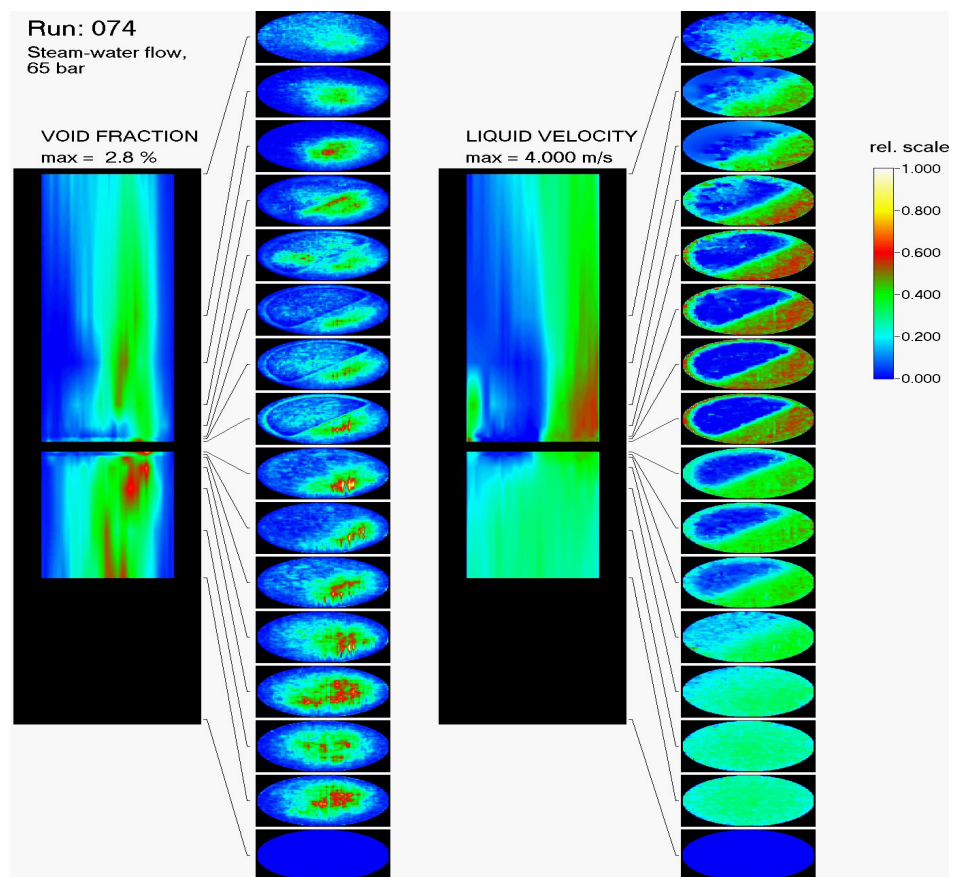

Figure 3: Void fraction and liquid velocity distributions in the steam-water test 6.5 MPa.

It is a surprising observation, that these gas bubbles are not able to enter the high-velocity region of the jet coming from the unobstructed part of the cross-section. At the greatest available distance downstream of the obstacle, a clearly separated, almost bubble-free round region is found that corresponds to the shape of the jet region. The latter mentioned bubble-free spot was not found in high-pressure steam-water experiments at similar superficial velocities (Figure 3). In general, both void fraction and velocity profiles show many points of similarity in the test with steam-water mixture compared to the air-water experiment. This concerns the flow behaviour at the stagnation point, the recirculation region, the jet formation and the gas accumulation. Differences are in particular, the absence of a wall peak and of the bubble-free spot far downstream of the obstacle.

A possible explanation is the hypothesis that the lift force pushes bubbles out of a region with a steep positive velocity gradient at its boundary. It is well-known, that the lift force changes sign with growing bubble diameter. Obviously, in case of the air-water flow, most of the bubbles experience a lift force characteristic for small bubbles. With growing pressure and temperature, the critical bubble diameter, where the lift force inverse takes place, is shifted towards much smaller bubble diameters (Tomiyama et al. (1995) and Tomiyama et al. (1998)). This might be the reason for the absence of the bubble-free spot in the steam-water test.

Lateral bubble velocities

Plots of the lateral velocity components in x and y directions show the deviation of the flow around the obstacle (Figures 4, 5, and 6 along with CFX simulation results). The vectors in these figures represent the average velocity of the instantaneous cross-sections of all bubbles in the time interval when they pass the measuring plane. The data of the air-water test point 074 is presented. For a better visualization the colour of the vectors indicates the relative value of the lateral velocities in each cross section (relative values between different cross sections are not to compare). Blue means minimal and red maximal velocities.

At z=-520 mm upstream of the obstacle (Figure 4), the vector field is dominated by a statistical scattering of the velocities except at the periphery of the pipe cross-section, where an unphysical tendency to deliver velocity vectors that point in a radial outwards direction is found. Since the influence of the obstacle starts to be recognizable only at about z = -160 mm, it can be assumed that there is a parallel flow at this distance. The outwards pointing vectors are therefore to be considered the result of a systematic measuring error. At z = -160 mm upstream of the obstacle (Figure 4), a pronounced lateral fluid movement from the obstructed to the unobstructed side of the pipe starts to develop. It becomes more and more intensive the more the obstacle is approached. Soon the diverging flow pattern caused by the stagnation point starts to become visible on the obstructed side. At the closest distance of z = -10 mm (Figure 4), the contour of the half-moon shaped plate is clearly reflected in the vector plot. The latter is found even in a more pronounced way in the vector fields closely downstream of the obstacle (Figure 5). On the unobstructed side, the vectors continue to point away from the obstacle still until z =+40 mm, where for the first time the vectors inverse. This corresponds to the shape of the jet found on the unobstructed side, which is bended towards the free side of the cross-section closely after the flow separation and later towards the obstructed side (see figure 2). Downstream the obstacle diverging velocities are found, too. They correspond to another stagnation point at the backside of the obstacle. This is a clear indication for a downwards flow in the wake of the half-moon plate and confirms the hypothesis of a recirculation in this region. At z = +160 mm, the vector field turns to a converging one, because this is the upper end of the recirculation region. At the two last measuring positions z = +250 and +520 mm (Figures 6, 7), there is a dominating flow from the unobstructed towards the obstructed side of the pipe cross-section. That is due to equilibrium re-establishment of the velocity profile, which was not reached again within the available range of the obstacle translation in none of the tests.
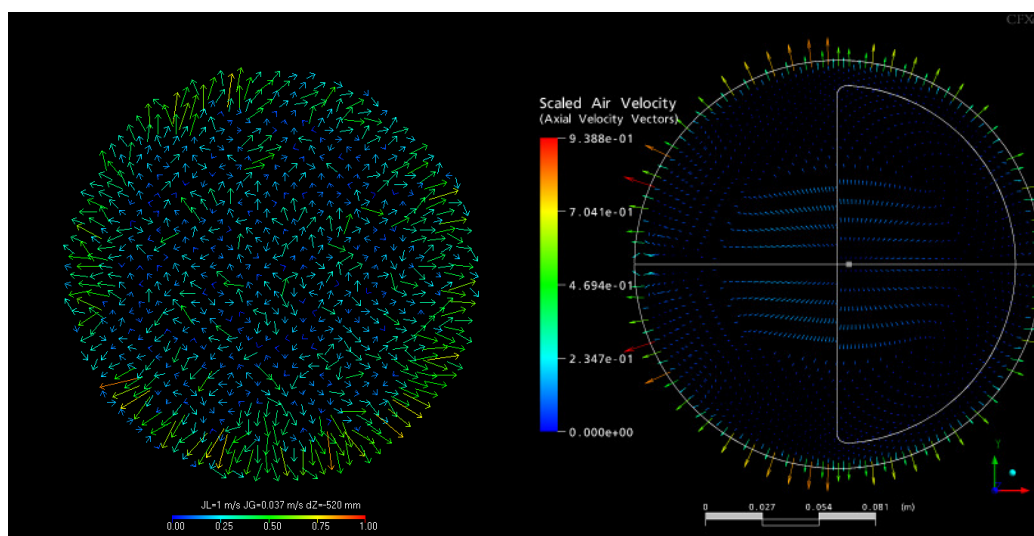

Figure 4: lateral bubble velocities, left (experimental), right (CFX calculation) for test point 074, at -520 distance upward the obstacle.
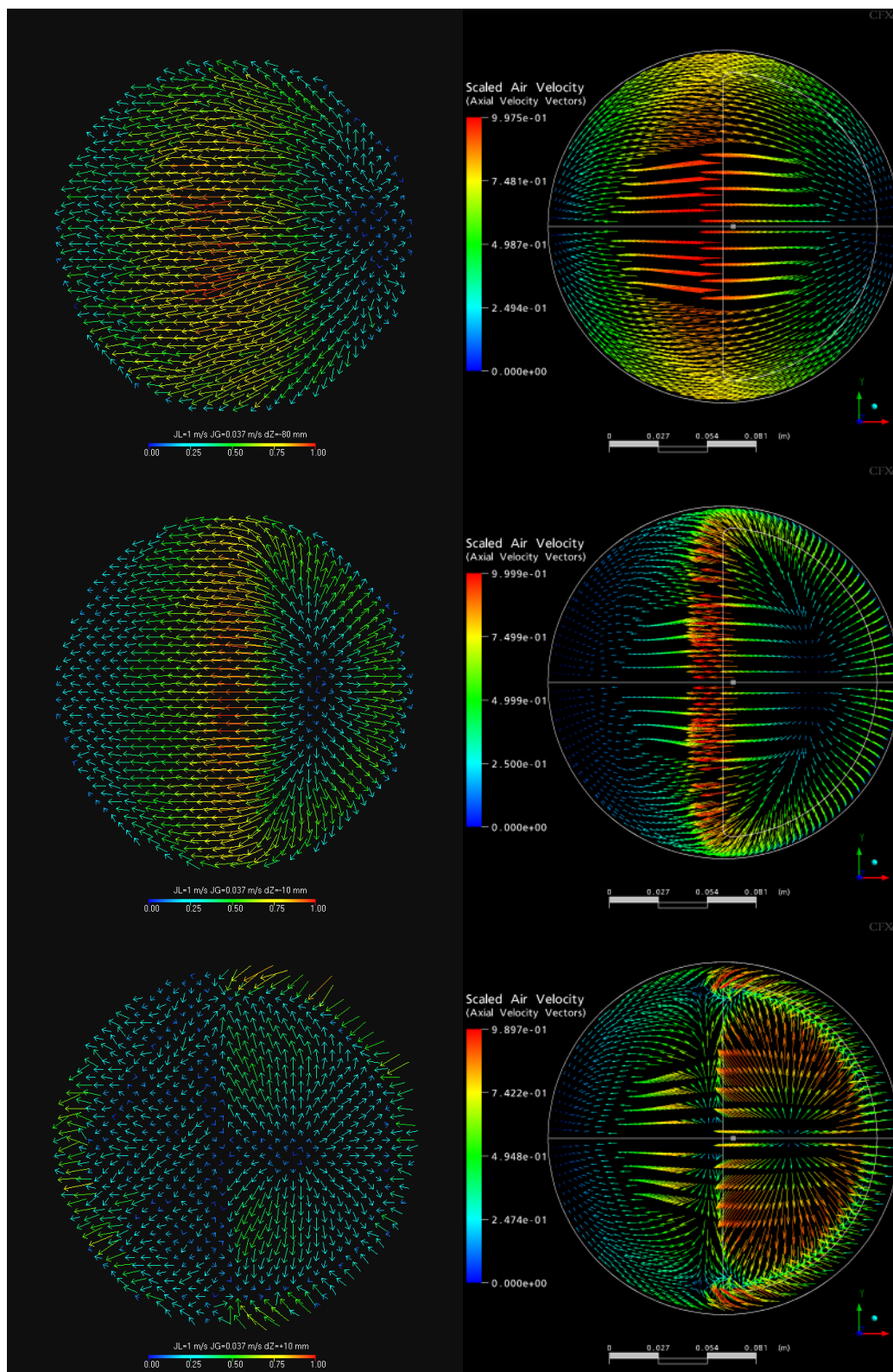
Figure 5: lateral bubble velocities, left (experimental), right (CFX calculation) for test point 074, at (from top to bottom) -80, and -10 mm distances upward the obstacle as well as +10 mm downwards the obstacle.
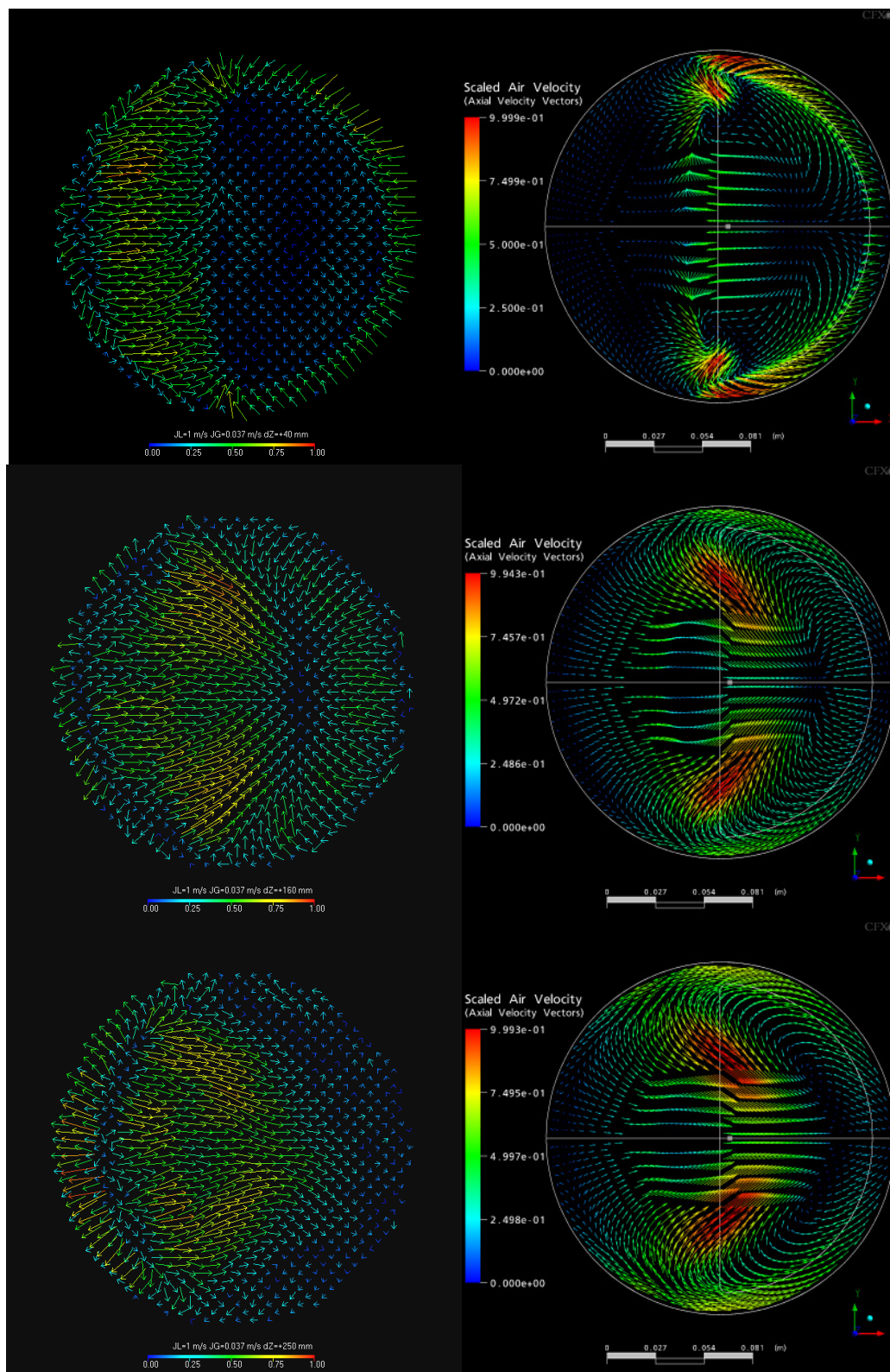
Figure 6: Lateral bubble velocities, left (experimental), right (CFX calculation) for test point 074, at (from top to bottom) +40, +160, +250 mm distances downward the obstacle.
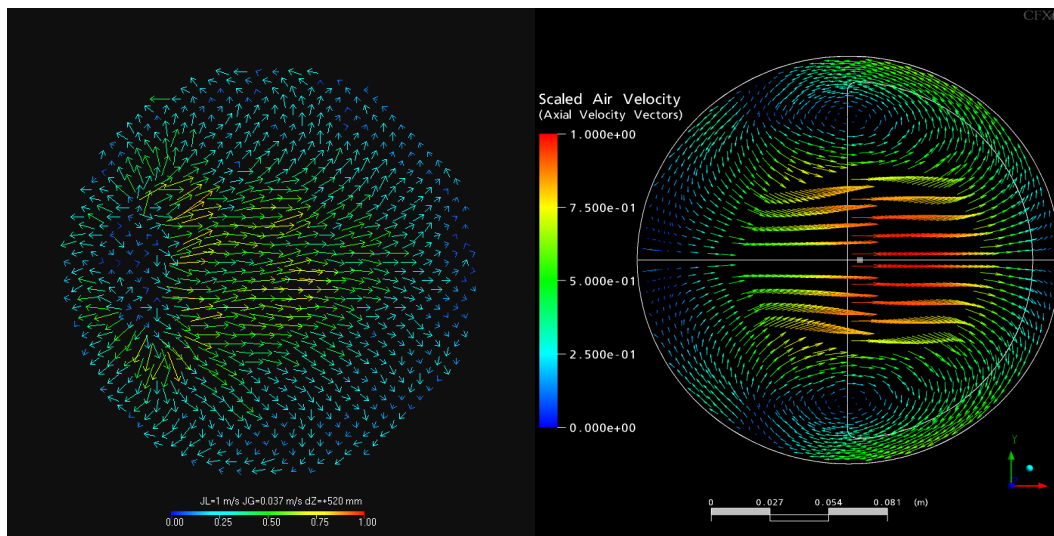
Figure 7: Lateral bubble velocities, left (experimental), right (CFX calculation) for test point 074, at +520 mm distance downward the obstacle.

Using the assumption that the lateral movement of the bubbles relative to the liquid can be neglected due to the domination of the bubble rise, a vector field of the liquid velocity in the vertical mid-plane of the pipe perpendicular to the linear edge of the half-moon shaped obstacle can be constructed by combining the lateral and the axial velocities. The result for the air-water test point 074 is shown in figure 8. The axial velocity components in the recirculation region were inverted manually.

This operation was limited to a region that is surrounded by a belt where the velocity is found to be close to zero. The spatial resolution of the vector plot was reduced compared to the resolution of the wire-mesh sensor by factor of two in order to keep the picture transparent. The overall structure of this field is typical for all test runs with equal superficial liquid velocities. For smaller superficial liquid velocities, the vector plots are much more affected by noise, which makes the interpretation difficult.
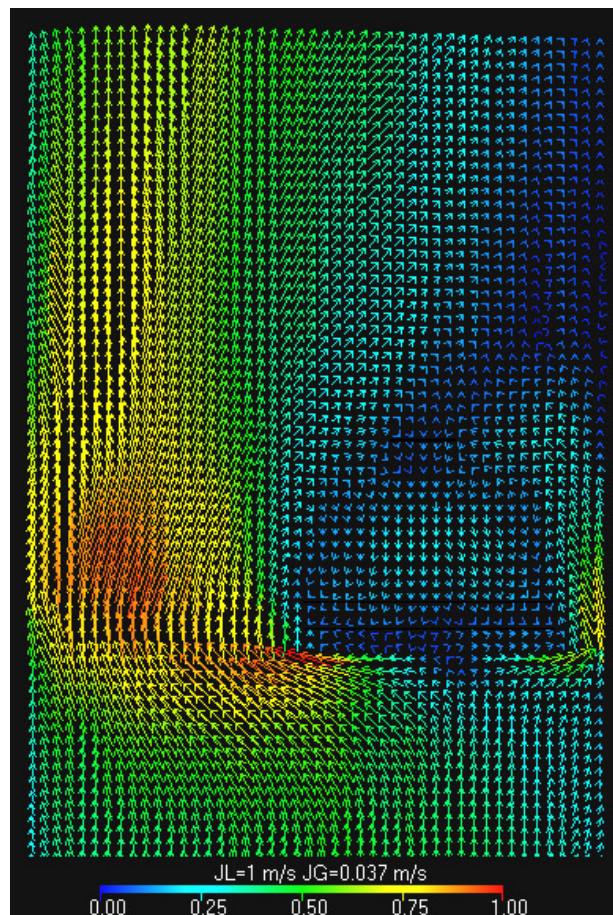

Figure 8: Velocity vector plot in a vertical symmetry plane around the obstacle for test point 074.

Result of the CFX Pre-Test Calculation

The steady-state ANSYS CFX calculations have well reproduced all details of the structure of the two-phase flow field around the obstacle for test conditions of TOPFLOW 074, (see figures. 4-7 previous chapter, and figure 9). This concerns shape and extension of the recirculation area, the stagnation zone upstream of the obstacle as well as the velocity and void fraction maxima in the non-obstructed part of the cross-section. Smaller details, like the velocity and void fraction maxima above the gap between the circular edge of the obstacle and the inner wall of the pipe are also found in a good agreement between experiment and calculation.

The 3D dataset from the wire-mesh sensor has been imported into the CFX graphical postprocessor in order to allow for the application of identical data processing, colour schemes and therefore a more direct comparison of the CFD results and experimental data. Since experimental data have a fine spatial resolution in the x-y-plane but a limited coarser resolution in z-direction, a pre-interpolation of the experimental data in z-direction has been applied with an axial resolution of the interpolated data with $\Delta z=1mm$.

A comparison of ANSYS CFX pre-test calculations on the finer grid with measurement data are shown in figure 9 for absolute axial water velocity and gas volume fraction distributions. The velocity field behind the obstacle shows the same location and intensity of the recirculation zone and stagnation regions on the obstacle surface. The reattachment length of the flow to the pipe wall downstream the obstacle is slightly increased in the CFD simulation, which is probably linked to the higher amount of entrained gas void fraction in the vortex behind the obstacle. Furthermore the present simulation tends to over predict the void fractions in the wake. This is a result of the assumption of a mono-disperse bubbly flow with a bubble size differing from reality and neglecting bubble coalescence and break-up with formation of larger bubbles in the wake of the obstacle. The agreement can be improved by using measured bubble-size distributions from the region upstream of the obstacle as a boundary condition for post-test calculations or by application of the inhomogeneous MUSIG model for the prediction of bubble size distributions from local flow conditions.
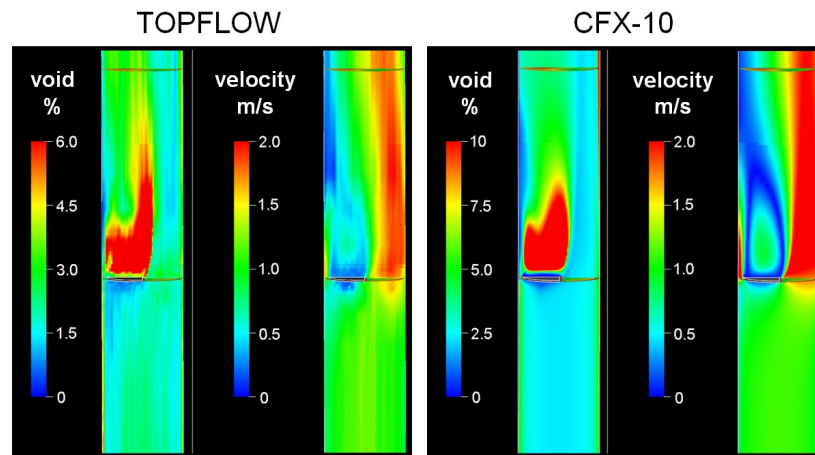

Figure 9: Experiment and CFX pre-test calculation by comparison of time averaged void fraction and axial liquid velocity distributions up- and downstream of the obstacle in the air-water test point.

Uncertainty overview of the velocity assessments:

The reconstructed superficial liquid velocity calculation depends on calibration factor in equation (13), which is not perfectly constant along axial direction. Reconstruction of the superficial liquid velocity gives an idea about the accuracy of calculated axial liquid velocity. Closely upstream of the obstacle, the inhomogeneous pressure field generates systematic measuring errors that affect the integral superficial velocity. In the recirculation region behind the obstacle, the reconstructed values are by about 20 % higher than the superficial velocity corresponding to the water volume flow (Figure 10). Further downstream, the reconstructed superficial liquid velocity falls back (-20 %) even below the value arising for the water supply.

A second important contribution to the systematic measuring error of axial velocity is the strong acceleration or, respectively deceleration of the flow close to the obstacle. The liquid velocity deduced from the marker bubble velocity minus the bubble rise velocity is relative to a stagnant liquid. If the flow experiences a strong acceleration, the real bubble velocity relative to the water phase may significantly deviate from this value. The additional pressure gradient amplifies the hydrostatic pressure gradient and an increase of the relative bubble rise velocity is observed.
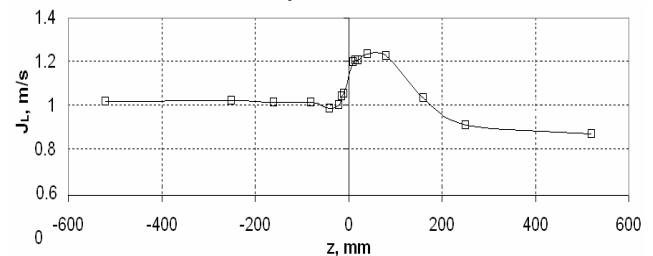

Figure 10: Reconstructed superficial liquid velocities as a function of the distance between obstacle and sensor for $J_L=1.017$ m/s and $J_G=0.0898$ m/s.

To estimate this effect a comparison was made between the liquid velocity distribution calculated by CFX with a the simulated measuring result, obtained from the calculated gas velocity distribution by subtracting the constant bubble rise velocity of 0.235 m/s. CFX calculation were performed with

mono-disperse bubbles of 5 mm diameter.
The result is shown in Figure 11, the error bars point at the real calculated axial liquid velocities. It is clearly visible, that the acceleration effects do not deteriorate the distribution in a qualitative way. It is concluded that the marker bubble method can lead to systematic errors caused by acceleration, which are in the range of 10-20 % of the amplitude of the velocity profiles.
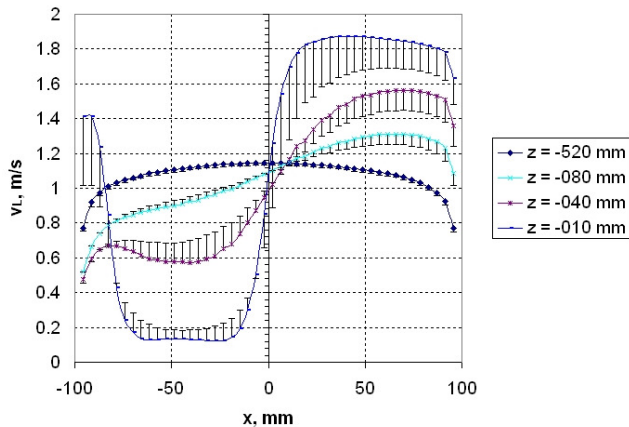

Figure 11: Lateral profiles of the simulated measured axial liquid velocity at selected axial positions upstream of the obstacle and bars for the systematic error caused by deceleration, assessed on basis of the CFX pre-test calculation, point 074.

For lateral bubble velocities the position z=520 mm upstream the obstacle was considered as reference. At this position the flow can be envisaged as axis-symmetric. The lateral components of the bubble velocity should equal to zero. Elliptically deformed bubbles that have a preferable inclination of their semi minor axis against the pipe wall cause an apparent lateral velocity component that is directed towards the wall. This is due to the fact that the centre of mass of the part of the measuring plane that is occupied by the bubble moves towards the wall, when the bubble passes through the sensor plane, even if the bubble itself moves in a vertical direction parallel to the z-axis. The resulting velocities are in the order of 0.1 - 0.2 m/s, as shown in Figure 12. Profiles of the lateral velocity component perpendicular to the linear edge of the obstacle for z = -40 mm show a strong lateral movement of the fluid from the obstructed towards the non-obstructed side that is significantly stronger than the error caused by the systematic bubble deformation effect.
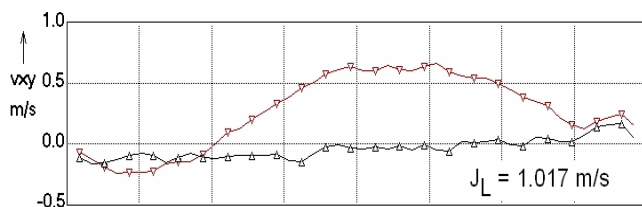

Figure 12: Lateral velocity along the diameter oriented perpendicularly to the linear edge of the half-moon shaped obstacle for two different upstream distances, $J_G = 0.0898$ m/s, red: z=-520 mm, black: z=-40 mm.

Conclusions

The two-phase flow field around an asymmetric obstacle in a vertical pipe is reconstructed using new techniques that allow producing data for CFD code validation in complex geometries. Main advantage is a translation of the obstacle to scan the 3D void field with a stationary wire-mesh sensor. Besides time-averaged void fraction field, a novel data evaluation method was developed to reconstruct 3D liquid velocity profiles from the wire-mesh sensor data.

The flow around an obstacle of the chosen geometry has many topological similarities with complex flow situations in bends, T-junctions, valves, safety valves and other components of power plant equipment and flow phenomena like curved stream lines, which form significant angles with the gravity vector, flow separation at sharp edges and recirculation zones in their wake are present. It is the goal of the ongoing CFD code development to accurately model such phenomena in a two-phase flow. Therefore, the experiments provide a good basis for the test and the validation of the codes and their underlying multiphase flow and turbulence models. Due to the generalizing capability of CFD codes, that can adapt to different geometric boundary conditions by the mesh generation, a successful validation on the kind of obtained experimental data guarantees the applicability of the code to other equally complex flow fields. A pre-test calculation done by ANSYS CFX 10.0 resulted in a good agreement with the experiment in terms of all significant qualitative details of the void fraction and velocity distributions. The structure and the geometry of the entire flow field in general as well as the dimensions of recirculation and stagnation zones in particular were predicted in good agreement with the experiment. It is planned to continue with post-test calculations in order to achieve a better quantitative agreement by using measured bubble-size distributions from the region upstream of the obstacle as inlet boundary condition and in a further step by applying the inhomogeneous MUSIG model for the prediction of bubble size distribution and bubble coalescence. The experimental data will be used to validate this recently developed and implemented model against detailed bubble size and bubble scale resolved void fraction measurements.

Acknowledgements

References

Ahmed, W.H., Ching, C.Y., Shoukri, M., (2005). Development of void fraction and liquid Turbulence of two phase flow downstream of sudden expansions, 4th International Conference on Transport Phenomena in Multiphase systems, Gdansk Poland.

Anagnostopoulos, J., Mathioulakis, D.S., (2004). A flow study around a time dependent 3-D asymmetric constriction. Journal of Fluids and Structures, Volume 19, Issue 1, 49-62.

ANSYS CFX 10.0, Users Manual (2005).ANSYS Inc.

Boccardi, G., Bubbico, R., Celata, G.P., Cumo, M., Di Tosto, F., (2004). Geometry Influence on Two-Phase Flow in Safety Valves. 5th International Conference of Multiphase Flow, ICMF'04, Yokohama, Japan, paper #478.

Founti, M., Klipfel, A., (1998). Experimental and computational investigations of nearly dense two-phase sudden expansion flows. Experimental Thermal and Fluid Science, Volume 17, Issues 1-2, 27-36.

Founti, M.A., Kolaitis, D.I., Katsourinis, D.I., (2001). Particle induced erosion wear in a sudden expansion flow and in a long pipe transporting crude oil. ASME Fluids Engineering Division Summer Meeting, New Orleans, Louisiana, USA.

Frank, Th., Shi, J., Burns, A.D., (2004). Validation of Eulerian multiphase flow models for nuclear reactor safety applications. 3rd TPFMI, Pisa, Italy, 1-8.

Frank Th., Advances in Computational Fluid Dynamics (CFD) of 3-dimensional gas-liquid multiphase flows, NAFEMS Seminar "Simulation of Complex Flows (CFD), Wiesbaden, Germany, April 25-26, (2005), pp. 1-18.

Frank, Th., (2006). Abschlussbericht zum Forschungsvor-haben 150 1271; Entwicklung von CFD-Software zur Simulation mehrdimensionaler Strömungen im Reaktor-kühlsystem. ANSYS Germany, Technical Report TR-06-01, 1-72.

Kondo, K., Yoshida, K., Okawa, T., Kataoka, I., (2002). Flow patterns of gas-liquid two-phase flow in round tube with sudden expansion. 10th International Conference on Nuclear Engineering, ICONE10, Arlington, VA, USA.

Kondo, K., Yoshida, K., Okawa, T., Kataoka, I., (2004). Prediction of void fraction distribution for turbulent bubble flow in a vertical pipe with sudden expansion. 3rd International Symposium on Two-Phase Flow Modeling and Experimentation, Pisa.

Kondo, K., Yoshida, K., Okawa, T., Kataoka, I., (2005). A study on bubble motion in turbulent flow field for predicting multi-dimensional void fraction distribution in sudden expansion channel, 13th International Conference on Nuclear Engineering Beijing, China, ICONE13-50644.

Morel, C., Pouvreau, J., Laviéville, J., Boucker, M., (2004). Numerical simulation of a bubbly flow in a sudden expansion with the NEPTUNE Code. 3rd International Symposium on Two-Phase Flow Modelling and Experimentation, Pisa.

Nishimura, M., Itoh, G., Furukawa, S., Takeshima, K., (2000). Development of Large capacity Main Steam Isolation Valves and Safety Relief Valves for next Generation BWR Plant.

Ota, T., Takeuchi, E., Yoshikawa, H., (2001). LES of three-dimensional turbulent separated reattached flow around a surface-mounted square plate. ASME Fluids Engineering Division Summer Meeting, New Orleans, Louisiana, USA.

Pietruske, H., Prasser, H.-M., (2005). Wire-mesh sensors for high-resolving two phase flow studies at high pressures and temperatures. NURETH-11, Avignon, France, paper #533, Flow Measurement Instrumentation (2007).

Prasser, H.-M., Scholz, D., Zippe, C., (2001). Bubble size measurement using wire-mesh sensors. Flow Measurement and Instrumentation, 12/4, 299-312.

Prasser, H.-M., Krepper, E., (2004c). Air water flow in a vertical pipe with sudden changes off the superficial water velocity. 3rd International Symposium on Two-Phase Flow Modelling and Experimentation, Pisa, Italy.

Prasser, H.-M., Beyer, M., Böttger, A., Carl, H., Lucas, D., Schaffrath, A., Schütz, P., Weiss, F.-P., Zschau, J., (2005a). Influence of the pipe diameter on the structure of the gas-liquid interface in a vertical two-phase pipe flow. Nuclear Technology. 152, 3-22.

Prasser, H.-M., Beyer, M., Carl, H., Pietruske, H., Schütz, P., (2005b). Steam-water experiments at high pressure to study the structure of the gas-liquid interface in a large vertical pipe. Annual Meeting on Nuclear Technology, Nuremberg, paper #215.

Rinne, A., Loth, R., (1996). Development of Local Two-Phase Flow Parameters for Vertical Bubbly Flow in a Pipe with Sudden Expansion. Experimental Thermal and Fluid Science, Volume 13, Issue 2, 152-166.

Schaffrath A., Krüssenberg A.-K., Weiss F.-P., Hicken E. F., Beyer M., Carl H., Schuster J., Schuetz P., Tamme M., (2001), TOPFLOW - a new multipurpose thermal hydraulic test facility for the investigation of steady state and transient two-phase flow phenomena, Kerntechnik, 66(2001)4, pp. 209-212.

Sotiriadis, A.A., Thorpe, R.B., (2005). Liquid re-circulation in turbulent vertical pipe flow behind a cylindrical bluff body and a ventilated cavity attached to a sparger. Chemical Engineering Science, Volume 60, Issue 4, 981-994.

Tomiyama, A. Sou, I. Zun, N. Kanami, T. Sakaguchi, (1995). Effects of Eötvös number and dimensionless liquid volumetric flux on lateral motion of a bubble in a laminar duct flow, Advances in Multiphase Flow, pp. 3-15.

Tomiyama, A., (1998) Struggle with computational bubble dynamics, in: Proceedings of Third International Conference on Multiphase Flow, ICMF 98, Lyon, France, June 8-12.